

# Hybrid origins of the cosmic-ray nuclei spectral hardening at a few hundred GV

Jia-Shu Niu<sup>1,2,\*</sup>

<sup>1</sup>*Institute of Theoretical Physics, Shanxi University, Taiyuan 030006, China*

<sup>2</sup>*State Key Laboratory of Quantum Optics and Quantum Optics Devices, Shanxi University, Taiyuan 030006, China*

Many experiments have confirmed the spectral hardening at a few hundred GV of cosmic-ray (CR) nuclei spectra, and 3 general different origins have been proposed: the primary source acceleration, the propagation, and the superposition of different kinds of sources. Here we report some new findings from the AMS-02 nuclei spectra of B and its dominating parents species (C, N, O, Ne, Mg, and Si): the nuclei spectral hardening in a few hundred GV should have hybrid origins. Besides the propagation origin, the superposition of different kinds of sources are also needed for different kinds of the CR primary nuclei species. All these results can be further confirmed by more precise CR nuclei spectra data in high rigidity regions (like that from DAMPE), and could provide us an opportunity to improve the current CR models.

## MOTIVATION

Many space-borne and ground-based experiments have confirmed the spectral hardening at a few hundred GV in cosmic-ray (CR) nuclei species (such as ATIC-2 [1], CREAM [2], and PAMELA [3]). The space station experiment Alpha Magnetic Spectrometer (AMS-02) improves the measurement precision of the CR fluxes by an order of the systematics [4] and leads us to a precision-driven era. The released spectra of different nuclei species by AMS-02 (including the primary CR species: proton [5], helium (He), carbon (C), oxygen (O) [6], neon (Ne), magnesium (Mg), silicon (Si) [7], and iron (Fe) [8]; the secondary CR species: lithium (Li), beryllium (Be), boron (B) [9], and fluorine (F) [10]; the hybrid CR species: nitrogen (N) [11], sodium (Na), and aluminum (Al) [12] provide us an excellent opportunity to study the origin, acceleration and propagation of CRs. As the most obvious and attractive fine structure in AMS-02 nuclei spectra, the spectral hardening in the region of 100 – 1000 GV has been studied by many works.

One of the most promising scenario (such as in Refs. [13–25]) proposes that the spectral hardening comes from the CR propagation process. Phenomenally, in such scenario, the secondary nuclei spectra should harden even more than that of the primary ones at a few hundred GV<sup>1</sup>, which is equivalent to add an extra high-rigidity break in the diffusion coefficient. In such configuration, some previous works show that AMS-02 nuclei data favors the hardening coming from the propagation process rather than the CR source injection in a statistical meaning (see, e.g., Refs. [18, 26]).

However, some recent works show that it is not that natural to conclude the propagation origin of the hardening (see, e.g., Refs. [27, 28]). Because the secondary

CR species (such as Li, Be, and B) are produced in collisions of primary CR particles (such as C, N, and O) with interstellar medium (ISM), the spectral hardening of the secondary CR species inherits from that of the CR primary species. The test of such process should consider all the parents species' contributions, at least the dominating ones.

In detail, the flux contribution of C to B is about 20%, which is almost equal to N but less than O [29]. In Ref. [28], it shows that not only the break rigidity (at a few hundred GV), but also the differences between the spectral index less and greater than the break of the spectra of C, N, and O are different. In such a case, the conclusions obtained from B/C ratio alone cannot represent the real propagation process completely (such as in Ref. [18, 30]). Moreover, the spectra of proton and He have very small uncertainties because of the extremely large event number, if one uses these spectra in the global fitting without employing independent injection spectra for them, they would seriously dilute the impacts of the real parents species' spectra (like that of C, N, O, Ne, Mg, and Si) on the daughter species' spectra (like that of Li, Be, and B) (such as in Refs. [23, 26]).

As a result, in this work, the AMS-02 CR nuclei spectra of C, N, O, Ne, Mg, and Si are used as the parents species, and that of B is used as the daughter species<sup>2</sup>. This clean data set could not only help us to check the consistency between the observed data and the CR model, but also avoid the systematics between different experiments. The data errors used in our fitting are the quadratic sum of statistical and systematic errors.

---

<sup>1</sup> The secondary species spectra not only inherit the hardening from the primary species (which is caused by the propagation of primary species), but are also hardened by their own propagation processes.

---

<sup>2</sup> The spectra of Li and Be are not used in this work because some recent works show that they might have extra primary components [23, 24, 26] and it needs to re-scale the production cross sections if we want to reproduce their spectra with that of B simultaneously [31, 32].

## SETUPS

A modified version of the diffusion-reacceleration scenario is used to describe the propagation process [33], which could successfully reproduce the spectra in low-rigidity regions and the diffusion coefficient is parameterized as

$$D_{xx}(R) = D_0 \cdot \beta^\eta \left( \frac{R_{\text{br}}}{R_0} \right) \times \begin{cases} \left( \frac{R}{R_{\text{br}}} \right)^{\delta_1} & R \leq R_{\text{br}} \\ \left( \frac{R}{R_{\text{br}}} \right)^{\delta_2} & R > R_{\text{br}} \end{cases}, \quad (1)$$

where  $R \equiv pc/Ze$  is the rigidity,  $\beta$  is the velocity of the particle in unit of light speed  $c$ ,  $R_{\text{br}}$  is the high-rigidity break,  $\delta_1$  and  $\delta_2$  are the diffusion slopes below and above the break, and  $R_0$  is the reference rigidity (4 GV).

The primary source injection spectra of all kinds of nuclei are assumed to be a broken power law form (with a low-rigidity break and a high-rigidity break) independently, which is represented as:

$$q_i \propto N_i \times \begin{cases} \left( \frac{R}{R_1^i} \right)^{-\nu_1^i} & R \leq R_1^i \\ \left( \frac{R}{R_1^i} \right)^{-\nu_2^i} & R_1^i < R \leq R_2^i \\ \left( \frac{R}{R_2^i} \right)^{-\nu_3^i} \left( \frac{R_2^i}{R_1^i} \right)^{-\nu_2^i} & R > R_2^i \end{cases}, \quad (2)$$

where  $i$  denotes the species of nuclei,  $N_i$  is the relative abundance of the species  $i$  to that of proton<sup>3</sup>, and  $\nu = \nu_1^i(\nu_2^i, \nu_3^i)$  for the nucleus rigidity  $R$  in the region divided by 2 breaks at the reference rigidity  $R_1^i$  and  $R_2^i$ . In this work, we use independent injection spectrum for C, N, O, Ne, Mg, and Si.<sup>4</sup> The nuclear network used in our calculations is extended to silicon-28.

The force-field approximation [34] is adopted to describe the effects of solar modulation in the solar system, which contains only one parameter the so-called solar-modulation potential  $\phi$ . All the above configurations are simulated and the diffusion equation are solved by the public code GALPROP v56<sup>5</sup> [35–39] numerically.<sup>6</sup>

It is necessary to note that in the model described above, the hardening in the spectra at a few hundred GV

TABLE I. Posterior mean and standard deviation of  $R_{\text{br}}^{\text{H}}$  and  $\Delta\nu^{\text{H}}$ .

ID	$R_{\text{br}}^{\text{H}}$ (GV)	$\Delta\nu^{\text{H}}$
$\delta$	$204 \pm 37$	$-0.12 \pm 0.03$
C	$230 \pm 99$	$-0.05 \pm 0.04$
N	$164 \pm 45$	$-0.32 \pm 0.09$
O	$825 \pm 126$	$-0.23 \pm 0.13$
Ne	$833 \pm 100$	$-0.39 \pm 0.18$
Mg	$389 \pm 135$	$-0.09 \pm 0.11$
Si	$461 \pm 249$	$0.05 \pm 0.14$

seems to be repeatedly contributed by the primary source acceleration ( $R_1^i, R_2^i, \nu_1^i, \nu_2^i, \nu_3^i$ ) and propagation process ( $R_{\text{br}}, \delta_1, \delta_2$ ). But the former will lead to an equal hardening of the primary and secondary spectra, while the latter will lead to a larger hardening in secondary spectra than in primary spectra. The fact whether the secondary nuclei spectra harden even more than that of the primary ones can be directly judged by the differences between  $\delta_1$  and  $\delta_2$ .

In total, we have the following 44 free parameters to determine via the data set

$$\boldsymbol{\theta} = \{D_0, \eta, R_{\text{br}}, \delta_1, \delta_2, z_h, v_A, | \\ N_C, R_1^C, R_2^C, \nu_1^C, \nu_2^C, \nu_3^C, | \\ N_N, R_1^N, R_2^N, \nu_1^N, \nu_2^N, \nu_3^N, | \\ N_O, R_1^O, R_2^O, \nu_1^O, \nu_2^O, \nu_3^O, | \\ N_{\text{Ne}}, R_1^{\text{Ne}}, R_2^{\text{Ne}}, \nu_1^{\text{Ne}}, \nu_2^{\text{Ne}}, \nu_3^{\text{Ne}}, | \\ N_{\text{Mg}}, R_1^{\text{Mg}}, R_2^{\text{Mg}}, \nu_1^{\text{Mg}}, \nu_2^{\text{Mg}}, \nu_3^{\text{Mg}}, | \\ N_{\text{Si}}, R_1^{\text{Si}}, R_2^{\text{Si}}, \nu_1^{\text{Si}}, \nu_2^{\text{Si}}, \nu_3^{\text{Si}}, | \\ \phi\}.$$

The Markov Chain Monte Carlo (MCMC) framework is used to determine the posterior probability distribution of the parameters (see, e.g., Refs. [23, 40]). The samples of the parameters are taken as their posterior probability distribution function (PDF) after the Markov Chains have reached their equilibrium states. The best-fit results and the corresponding residuals of the spectra are given in Appendix Figure 3. The best-fit values, statistical mean values and standard deviations for the parameters in  $\boldsymbol{\theta}$  are shown in Appendix Table II, and  $\chi^2/d.o.f = 80.64/422$  for the best-fit result.

The posterior mean and standard deviation of the high-rigidity break ( $R_{\text{br}}^{\text{H}} \equiv R_2^i$  for C, N, O, Ne, Mg, and Si;  $R_{\text{br}}^{\text{H}} \equiv R_{\text{br}}$  for  $\delta$ ) and the differences between the spectral index greater and less than them ( $\Delta\nu^{\text{H}} \equiv \nu_3^i - \nu_2^i$  for C, N, O, Ne, Mg, and Si;  $\Delta\nu^{\text{H}} \equiv \delta_2 - \delta_1$  for  $\delta$ ) are listed in Table I. The box plot<sup>7</sup> of these two kinds of parameters

<sup>3</sup> The relative abundance of proton is fixed to  $10^6$  and the post-propagated normalization flux of protons at 100 GeV is fixed to  $4.45 \times 10^{-2} \text{ m}^{-2} \text{ s}^{-1} \text{ sr}^{-1} \text{ GeV}^{-1}$ .

<sup>4</sup> Here, we use the injection spectra of the dominating isotopes  $^{12}\text{C}$ ,  $^{14}\text{N}$ ,  $^{16}\text{O}$ ,  $^{20}\text{Ne}$ ,  $^{24}\text{Mg}$ , and  $^{28}\text{Si}$  to represent that of the corresponding elements. All the other primary injection species who have small contributions on the flux of B are assumed to have the same injection spectra as  $^{20}\text{Ne}$ .

<sup>5</sup> <http://galprop.stanford.edu>

<sup>6</sup> More details about the configuration can be referred to in Refs. [23, 40].

<sup>7</sup> A box plot or boxplot is a method for graphically depicting

are shown in Figure 1.

## DISCUSSIONS AND CONCLUSION

In the left panel of Figure 1, the high-rigidity breaks show different distributions: for C and N, they distribute around 200 GV; for O and Ne, they distribute around 850 GV; for Mg and Si, they distribute quite widely among the above two cases. These different distributions of the high-rigidity breaks cannot be naturally reproduced by a uniform acceleration mechanism in the primary source injection spectra for different CR nuclei species. As some previous work have been pointed out (see, e.g., Refs. [28, 41–43]), it could be naturally explained by the superposition of different kinds of sources. In this scenario, each kind of the sources have similar spectral indexes for all the primary source injection but have different element abundances between different kinds of sources.<sup>8</sup> Moreover, the concentrated distribution of  $R_{br}^H$  for  $\delta$  infer that the data set has a quite strong constraint on it and the break of  $\delta$  is necessary.

In the right panel of Figure 1, except the distributions of  $\Delta\nu^H$  for C, Mg, and Si, that for the other species are smaller than 0 exceeding 95% confidence level. This result indicates that the breaks in the injection spectra of N, O, and Ne are necessary if we want to reproduce the high-rigidity hardening in these spectra. On the other hand, the concentrated distribution of  $\Delta\nu^H$  for  $\delta$  also shows its necessity to reproduce the data set, which has been proved by some of the previous works based on different configurations (see, e.g., [18, 26, 30]).

In summary, if we want to reproduce the spectral hardening in the CR nuclei species at a few hundred GV precisely, not only an extra break at about 200 GV in the diffusion coefficient is needed, but also the extra independent high-rigidity breaks in the primary source injection for different CR species are needed. The former could come from the propagation process (such as the spatial-dependent propagation, see, e.g., [14, 17, 45]), and the latter can be naturally explained by the superposition of different kinds of sources. Consequently, the CR nuclei spectral hardening at a few hundred GV has hybrid origins.

**Note:** In Figure 2 ( $\Delta\nu^L \equiv \nu_2^i - \nu_1^i$  for C, N, O, Ne, Mg, and Si), the distributions of  $\Delta\nu^L$  are around 0 and have large overlaps, which indicates that it is unnecessary

---

groups of numerical data through their quartiles. In our configurations, the band inside the box shows the median value of the dataset, the box shows the quartiles, and the whiskers extend to show the rest of the distribution which are edged by the 5th percentile and the 95th percentile.

<sup>8</sup> An interesting and detailed work on revealing the origin of galactic CRs by their composition has been proposed in Ref. [44].

to employ the low-rigidity breaks in the primary source injection to reproduce the observed CR spectra of these species (see, e.g., [46]).

## ACKNOWLEDGMENTS

This research was supported by the National Natural Science Foundation of China (NSFC) (No. 12005124) and the Applied Basic Research Programs of Natural Science Foundation of Shanxi Province (No. 201901D111043).

---

\* jsniu@sxu.edu.cn

- [1] A. D. Panov, J. H. Adams, and H. S. Ahn et al, ArXiv Astrophysics e-prints (2006), astro-ph/0612377.
- [2] H. S. Ahn, P. Allison, and M. G. Bagliesi et al, *Astrophys. J. Lett.* **714**, L89 (2010), arXiv:1004.1123 [astro-ph.HE].
- [3] O. Adriani, G. C. Barbarino, and G. A. Bazilevskaya et al, *Science* **332**, 69 (2011), arXiv:1103.4055 [astro-ph.HE].
- [4] M. Aguilar, G. Alberti, and B. Alpat et al, *Phys. Rev. Lett.* **110**, 141102 (2013).
- [5] M. Aguilar, D. Aisa, and B. Alpat et al, *Phys. Rev. Lett.* **114**, 171103 (2015).
- [6] M. Aguilar, L. Ali Cavasonza, and B. Alpat et al (AMS Collaboration), *Phys. Rev. Lett.* **119**, 251101 (2017).
- [7] M. Aguilar, L. Ali Cavasonza, and G. Ambrosi et al, *Phys. Rev. Lett.* **124**, 211102 (2020).
- [8] M. Aguilar, L. A. Cavasonza, M. S. Allen, and et al. (AMS Collaboration), *Phys. Rev. Lett.* **126**, 041104 (2021).
- [9] M. Aguilar, L. Ali Cavasonza, and G. Ambrosi et al (AMS Collaboration), *Phys. Rev. Lett.* **120**, 021101 (2018).
- [10] M. Aguilar, L. A. Cavasonza, M. S. Allen, and et al. (AMS Collaboration), *Phys. Rev. Lett.* **126**, 081102 (2021).
- [11] M. Aguilar, L. Ali Cavasonza, and B. Alpat et al (AMS Collaboration), *Phys. Rev. Lett.* **121**, 051103 (2018).
- [12] M. Aguilar, L. A. Cavasonza, B. Alpat, and et al (AMS Collaboration), *Phys. Rev. Lett.* **127**, 021101 (2021).
- [13] P. Blasi, E. Amato, and P. D. Serpico, *Phys. Rev. Lett.* **109**, 061101 (2012), arXiv:1207.3706 [astro-ph.HE].
- [14] N. Tomassetti, *Astrophys. J. Lett.* **752**, L13 (2012), arXiv:1204.4492 [astro-ph.HE].
- [15] N. Tomassetti, *Astrophys. J. Lett.* **815**, L1 (2015), arXiv:1511.04460 [astro-ph.HE].
- [16] N. Tomassetti, *Phys. Rev. D* **92**, 081301(R) (2015), arXiv:1509.05775 [astro-ph.HE].
- [17] J. Feng, N. Tomassetti, and A. Oliva, *Phys. Rev. D* **94**, 123007 (2016), arXiv:1610.06182 [astro-ph.HE].
- [18] Y. Génolini, P. D. Serpico, and M. Boudaud et al, *Phys. Rev. Lett.* **119**, 241101 (2017).
- [19] C. Jin, Y.-Q. Guo, and H.-B. Hu, *Chinese Physics C* **40**, 015101 (2016), arXiv:1504.06903 [astro-ph.HE].
- [20] Y.-Q. Guo and Q. Yuan, *Chinese Physics C* **42**, 075103 (2018), arXiv:1701.07136 [astro-ph.HE].

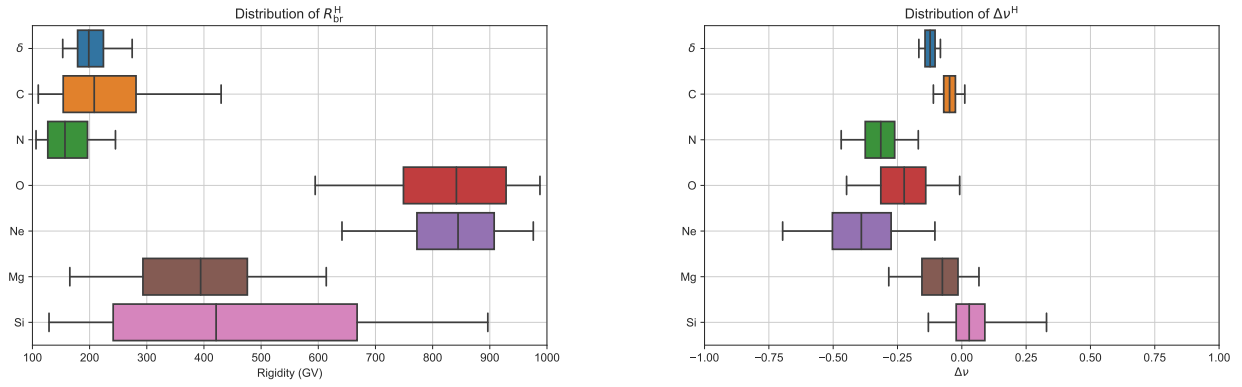


FIG. 1. Boxplots for the  $R_{br}^H$  and  $\Delta\nu^H$ . The band inside the box shows the median value of the dataset, the box shows the quartiles, and the whiskers extend to show the rest of the distribution which are edged by the 5th percentile and the 95th percentile.

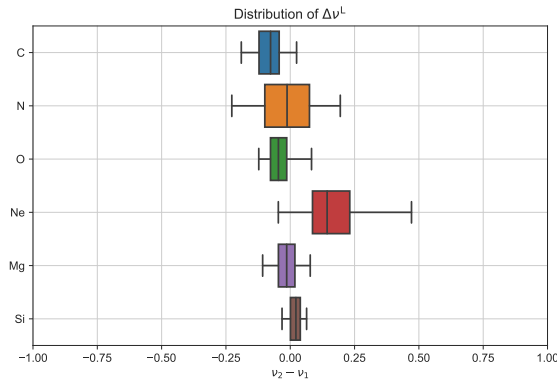


FIG. 2. Same as Figure 1, but for the  $\Delta\nu^L$ .

- [21] Y.-Q. Guo and Q. Yuan, *Phys. Rev. D* **97**, 063008 (2018), arXiv:1801.05904 [astro-ph.HE].
- [22] W. Liu, Y.-h. Yao, and Y.-Q. Guo, *Astrophys. J.* **869**, 176 (2018), arXiv:1802.03602 [astro-ph.HE].
- [23] J.-S. Niu, T. Li, and H.-F. Xue, *Astrophys. J.* **873**, 77 (2019), arXiv:1810.09301 [astro-ph.HE].
- [24] M. J. Boschini, S. Della Torre, M. Gervasi, D. Grandi, G. Jóhannesson, G. La Vacca, N. Masi, I. V. Moskalenko, S. Pensotti, T. A. Porter, L. Quadrani, P. G. Rancoita, D. Rozza, and M. Tacconi, *Astrophys. J.* **889**, 167 (2020), arXiv:1911.03108 [astro-ph.HE].
- [25] M. J. Boschini, S. Della Torre, M. Gervasi, D. Grandi, G. Jóhannesson, G. La Vacca, N. Masi, I. V. Moskalenko, S. Pensotti, T. A. Porter, L. Quadrani, P. G. Rancoita, D. Rozza, and M. Tacconi, *Astrophys. J. Supp.* **250**, 27 (2020), arXiv:2006.01337 [astro-ph.HE].
- [26] J.-S. Niu and H.-F. Xue, *J. Cosmol. Astropart. Phys.* **2020**, 036 (2020), arXiv:1902.09343 [astro-ph.HE].
- [27] Q. Yuan, C.-R. Zhu, X.-J. Bi, and D.-M. Wei, *J. Cosmol. Astropart. Phys.* **2020**, 027 (2020), arXiv:1810.03141 [astro-ph.HE].
- [28] J.-S. Niu, *Chinese Physics C* **45**, 041004 (2021), arXiv:2009.00884 [astro-ph.HE].
- [29] Y. Génolini, D. Maurin, I. V. Moskalenko, and M. Unger, *Phys. Rev. C* **98**, 034611 (2018), arXiv:1803.04686 [astro-ph.HE].
- [30] Y. Génolini, M. Boudaud, P. I. Batista, S. Caroff, L. Derome, J. Lavalle, A. Marcowith, D. Maurin, V. Poireau, V. Poulin, S. Rosier, P. Salati, P. D. Serpico, and M. Vecchi, *Phys. Rev. D* **99**, 123028 (2019), arXiv:1904.08917 [astro-ph.HE].
- [31] P. De La Torre Luque, M. N. Mazziotta, F. Loparco, F. Gargano, and D. Serini, *J. Cosmol. Astropart. Phys.* **2021**, 099 (2021), arXiv:2101.01547 [astro-ph.HE].
- [32] P. De La Torre Luque, M. N. Mazziotta, F. Loparco, F. Gargano, and D. Serini, *J. Cosmol. Astropart. Phys.* **2021**, 010 (2021), arXiv:2102.13238 [astro-ph.HE].
- [33] Q. Yuan, *Science China Physics, Mechanics, and Astronomy* **62**, 49511 (2019), arXiv:1805.10649 [astro-ph.HE].
- [34] L. J. Gleeson and W. I. Axford, *Astrophys. J.* **154**, 1011 (1968).
- [35] A. W. Strong and I. V. Moskalenko, *Astrophys. J.* **509**, 212 (1998), astro-ph/9807150.
- [36] I. V. Moskalenko, A. W. Strong, J. F. Ormes, and M. S. Potgieter, *Astrophys. J.* **565**, 280 (2002), astro-ph/0106567.
- [37] A. W. Strong and I. V. Moskalenko, *Advances in Space Research* **27**, 717 (2001), astro-ph/0101068.
- [38] I. V. Moskalenko, A. W. Strong, S. G. Mashnik, and J. F. Ormes, *Astrophys. J.* **586**, 1050 (2003), astro-ph/0210480.
- [39] V. S. Ptuskin, I. V. Moskalenko, F. C. Jones, A. W. Strong, and V. N. Zirakashvili, *Astrophys. J.* **642**, 902 (2006), astro-ph/0510335.
- [40] J.-S. Niu and T. Li, *Phys. Rev. D* **97**, 023015 (2018), arXiv:1705.11089 [astro-ph.HE].
- [41] Q. Yuan, B. Zhang, and X.-J. Bi, *Phys. Rev. D* **84**, 043002 (2011), arXiv:1104.3357 [astro-ph.HE].
- [42] C. Yue, P.-X. Ma, and Q. Yuan et al, *Frontiers of Physics* **15**, 24601 (2019), arXiv:1909.12857 [astro-ph.HE].
- [43] Q. Yuan, B.-Q. Qiao, Y.-Q. Guo, Y.-Z. Fan, and X.-J. Bi, *Frontiers of Physics* **16**, 24501 (2020), arXiv:2007.01768 [astro-ph.HE].
- [44] V. Tatischeff, J. C. Raymond, J. Duprat, S. Gabici, and S. Recchia, arXiv e-prints, arXiv:2106.15581 (2021),

- arXiv:2106.15581 [astro-ph.HE].
- [45] Y.-Q. Guo, Z. Tian, and C. Jin, *Astrophys. J.* **819**, 54 (2016).
- [46] M. Korsmeier and A. Cuoco, *Phys. Rev. D* **103**, 103016 (2021), arXiv:2103.09824 [astro-ph.HE].

## APPENDIX

Note that in the lower panel of subfigures in Fig. 3, the  $\sigma_{\text{eff}}$  is defined as

$$\sigma_{\text{eff}} = \frac{f_{\text{obs}} - f_{\text{cal}}}{\sqrt{\sigma_{\text{stat}}^2 + \sigma_{\text{syst}}^2}}, \quad (3)$$

where  $f_{\text{obs}}$  and  $f_{\text{cal}}$  are the points which come from the observation and model calculation;  $\sigma_{\text{stat}}$  and  $\sigma_{\text{syst}}$  are the statistical and systematic standard deviations of the observed points. This quantity could clearly show us the deviations between the best-fit result and observed values at each point based on its uncertainty.

TABLE II. Constraints on the parameters in set  $\theta$ . The prior interval, best-fit value, statistic mean, and standard deviation are listed for parameters. With  $\chi^2/d.o.f = 80.64/422$  for best-fit result.

ID	Prior range	Posterior mean & Standard deviation	Best-fit value
$D_0$ ( $10^{28} \text{ cm}^2 \text{ s}^{-1}$ )	[1, 20]	$5.6 \pm 0.6$	5.59
$\eta$	[-5.0, 5.0]	$-1.7 \pm 0.2$	-1.69
$R_{\text{br}}$ (GV)	[100, 1000]	$208 \pm 34$	207.68
$\delta_1$	[0.1, 1.0]	$0.46 \pm 0.02$	0.458
$\delta_2$	[0.1, 1.0]	$0.34 \pm 0.03$	0.338
$z_h$ (kpc)	[0.5, 20.0]	$8 \pm 1$	7.962
$v_A$ (km/s)	[0, 70]	$17 \pm 2$	16.77
$N_C$	[10, 6000]	$3389 \pm 48$	3389.8
$R_1^C$ (GV)	[1, 100]	$9 \pm 4$	9.05
$R_2^C$ (GV)	[100, 1000]	$220 \pm 82$	219.54
$\nu_1^C$	[1.0, 4.0]	$2.44 \pm 0.07$	2.437
$\nu_2^C$	[1.0, 4.0]	$2.36 \pm 0.01$	2.364
$\nu_3^C$	[1.0, 4.0]	$2.31 \pm 0.04$	2.314
$N_N$	[0, 80]	$252 \pm 13$	252.4
$R_1^N$ (GV)	[1, 100]	$15 \pm 9$	15.06
$R_2^N$ (GV)	[100, 1000]	$160 \pm 40$	160.44
$\nu_1^N$	[1.0, 4.0]	$2.42 \pm 0.10$	2.418
$\nu_2^N$	[1.0, 4.0]	$2.42 \pm 0.04$	2.418
$\nu_3^N$	[1.0, 4.0]	$2.10 \pm 0.08$	2.096
$N_O$	[0, 80]	$4285 \pm 52$	4285.3
$R_1^O$ (GV)	[1, 100]	$11 \pm 7$	10.81
$R_2^O$ (GV)	[100, 1000]	$833 \pm 108$	833.05
$\nu_1^O$	[1.0, 4.0]	$2.42 \pm 0.05$	2.421
$\nu_2^O$	[1.0, 4.0]	$2.38 \pm 0.01$	2.384
$\nu_3^O$	[1.0, 4.0]	$2.14 \pm 0.13$	2.142
$N_{\text{Ne}}$	[0, 80]	$501 \pm 9$	501.1
$R_1^{\text{Ne}}$ (GV)	[1, 100]	$6 \pm 3$	6.36
$R_2^{\text{Ne}}$ (GV)	[100, 1000]	$849 \pm 86$	849.15
$\nu_1^{\text{Ne}}$	[1.0, 4.0]	$2.20 \pm 0.17$	2.204
$\nu_2^{\text{Ne}}$	[1.0, 4.0]	$2.38 \pm 0.01$	2.382
$\nu_3^{\text{Ne}}$	[1.0, 4.0]	$1.98 \pm 0.17$	1.975
$N_{\text{Mg}}$	[0, 80]	$618 \pm 12$	617.82
$R_1^{\text{Mg}}$ (GV)	[1, 100]	$16 \pm 11$	16.44
$R_2^{\text{Mg}}$ (GV)	[100, 1000]	$392 \pm 110$	391.77
$\nu_1^{\text{Mg}}$	[1.0, 4.0]	$2.47 \pm 0.05$	2.472
$\nu_2^{\text{Mg}}$	[1.0, 4.0]	$2.46 \pm 0.01$	2.462
$\nu_3^{\text{Mg}}$	[1.0, 4.0]	$2.36 \pm 0.10$	2.357
$N_{\text{Si}}$	[0, 80]	$742 \pm 13$	742.2
$R_1^{\text{Si}}$ (GV)	[1, 100]	$47 \pm 17$	46.93
$R_2^{\text{Si}}$ (GV)	[100, 1000]	$428 \pm 207$	428.14
$\nu_1^{\text{Si}}$	[1.0, 4.0]	$2.42 \pm 0.02$	2.422
$\nu_2^{\text{Si}}$	[1.0, 4.0]	$2.44 \pm 0.02$	2.442
$\nu_3^{\text{Si}}$	[1.0, 4.0]	$2.48 \pm 0.12$	2.476
$\phi$ (GV)	[0, 1.5]	$0.81 \pm 0.04$	0.808

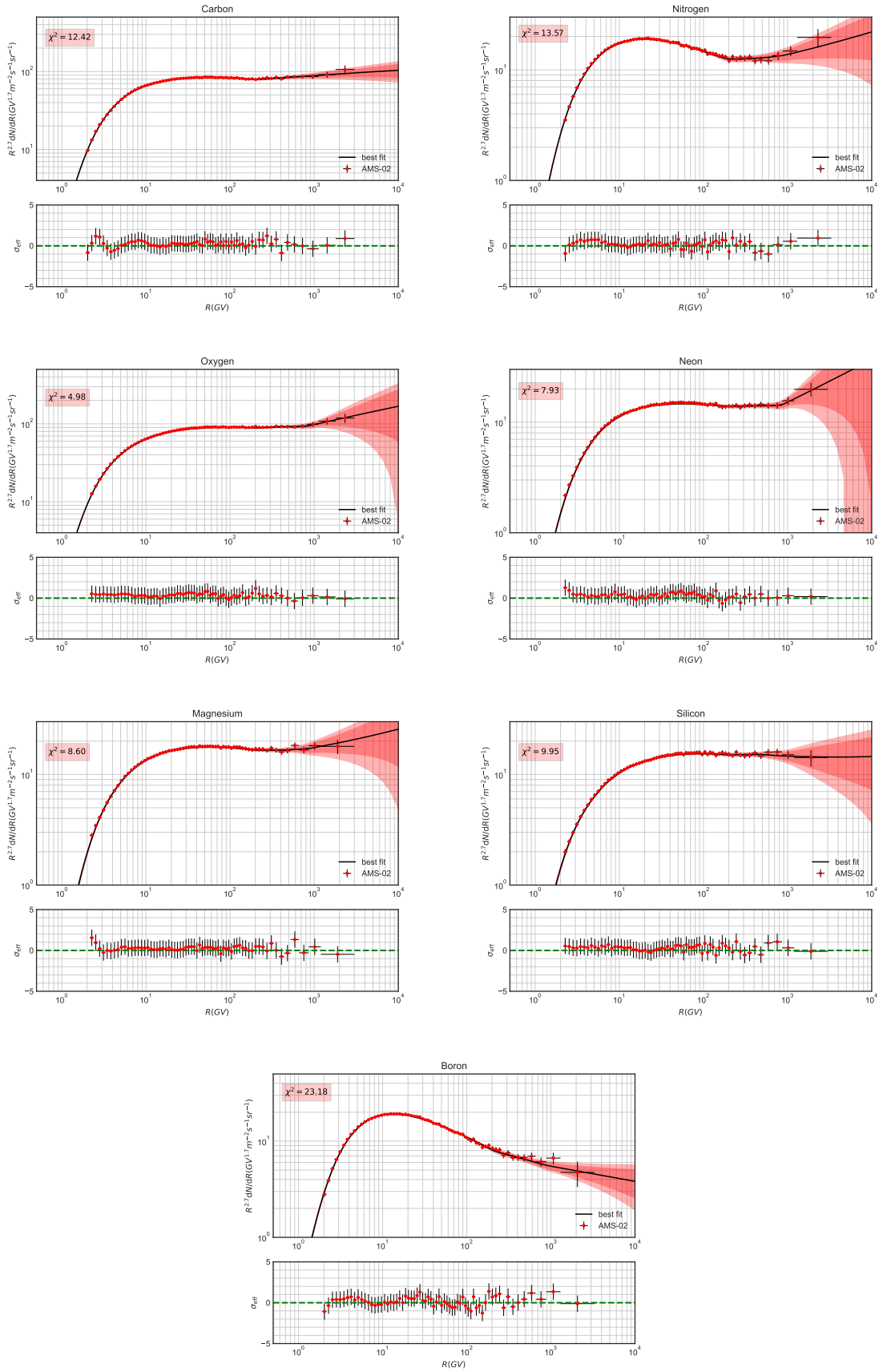


FIG. 3. Fitting results and corresponding residuals to the CR spectra of B and its parents' species (C, N, O, Ne, Mg, and Si). The  $2\sigma$  (deep red) and  $3\sigma$  (light red) bounds are also shown in the subfigures. The relevant  $\chi^2$  of each spectrum is given in the subfigures as well.